TABLE 13.1 Some Values of Constants for Time–Temperature Parameters[1]

Material	Sherby–Dorn Q kJ/mole	Larson–Miller C	Manson–Haferd T_a, K	Manson–Haferd log t_a
Various steels and stainless steels	≈400	≈20	—	—
Pure aluminum and dilute alloys	≈150	—	—	—
S-590 alloy (Fe base)	350	17	172	20
A-286 stainless steel	380	20	367	16
Nimonic 81A (Ni base)	380	18	311	16
1Cr-1Mo-0.25V steel	460	22	311	18

[1] Adapted from N. E. Dowling, *Mechanical Behavior of Materials* (Englewood Cliffs, NJ: Prentice Hall, 1993), p. 699, Table 15.1.

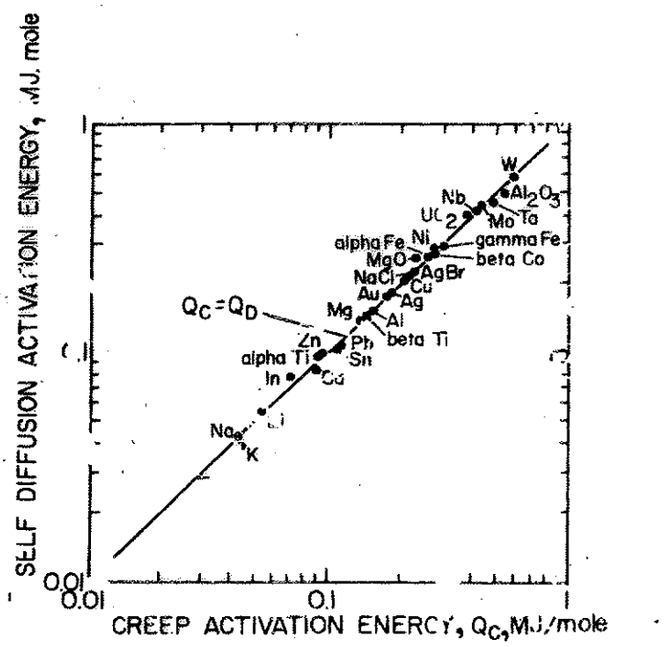

Figure 13.9 Activation energies for creep (stage II) and self-diffusion for a number of metals. (Adapted with permission from O. D. Sherby and A. K. Miller, *J. Eng. Mater. Technol.*, 101 (1979) 387)

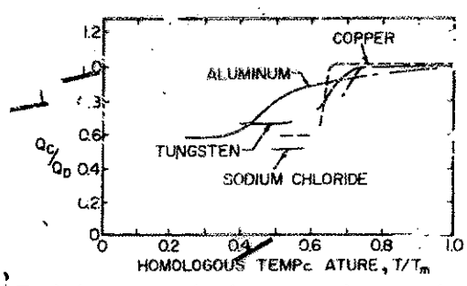

Figure 13.10 Ratio between activation energy for secondary creep and activation energy for bulk diffusion as a function of temperature. (Adapted with permission from O. D. Sherby and A. K. Miller, *J. Eng. Mater. Technol.*, 101 (1979) 387).

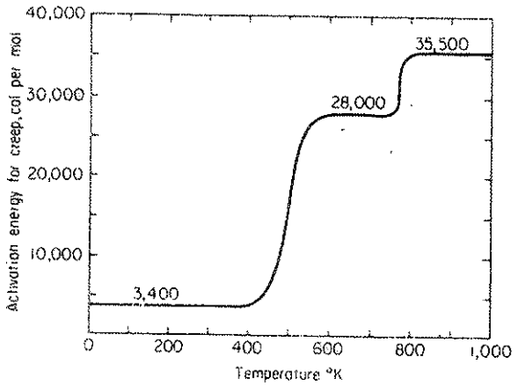

Fig. 13-10 Activation energy for creep in aluminum single crystals. (*From J. L. Lytton, L. A. Shepard, and J. E. Dorn, Trans. Metall. Soc. AIME, vol. 212, p. 220, 1958.*)

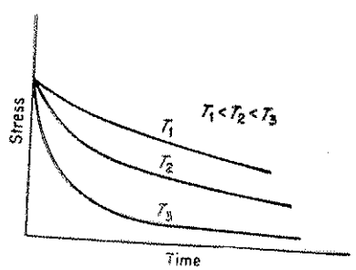

Fig. 13-21 Stress-relaxation curves.

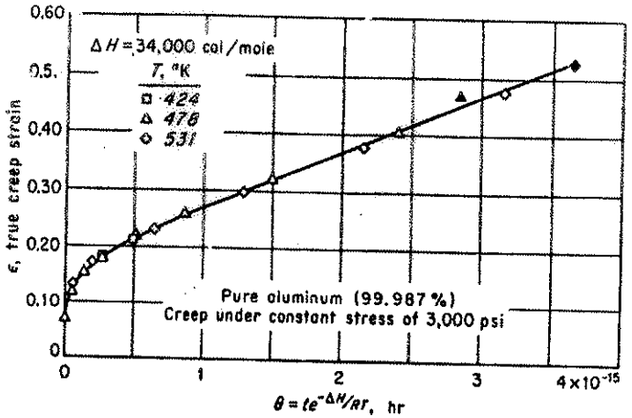

Fig. 13-8 Creep strain vs. $\theta = te^{-\Delta H/RT}$. (*From J. E. Dorn, in "Creep and Recovery," American Society for Metals, Metals Park, Ohio, 1957.*)

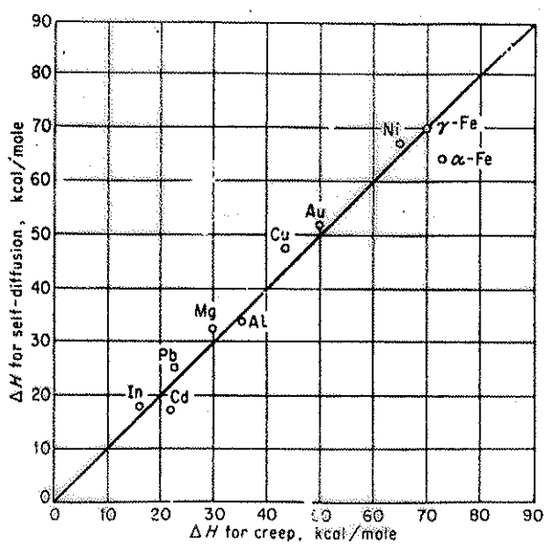

Fig. 13-9 Correlation between activation energies for high-temperature creep and self-diffusion. (*From J. E. Dorn, in "Creep and Recovery," p. 274, American Society for Metals, Metals Park, Ohio, 1957.*)

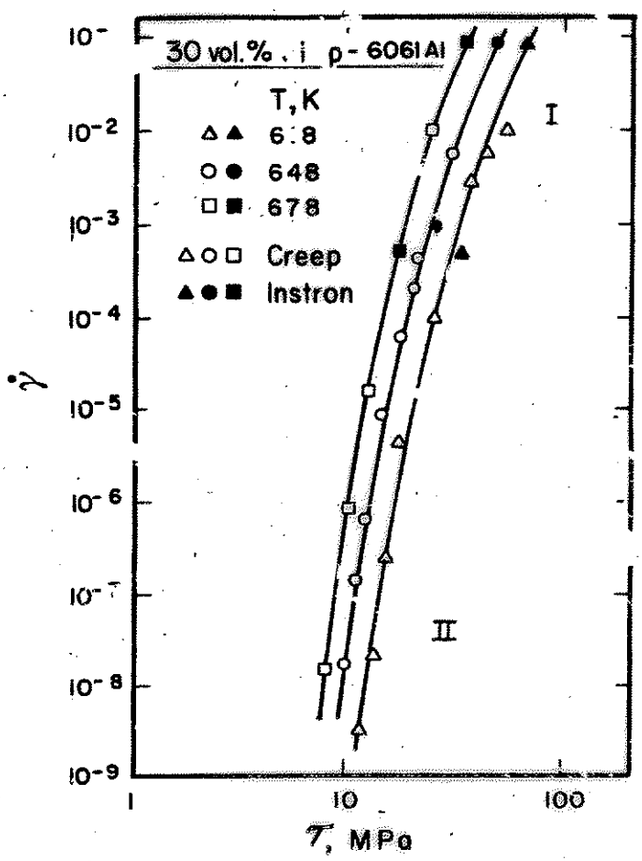

Figure 13.1 Shear stress vs. shear strain rate in an aluminum (6061) with 30 vol % SiC particulate composite in creep. (From K.-T. Park, E. J. Lavernia, and F. A. Mohamed, *Acta Met. Mat.*, 38 (1990) 2149, Figure 7, p. 2153)

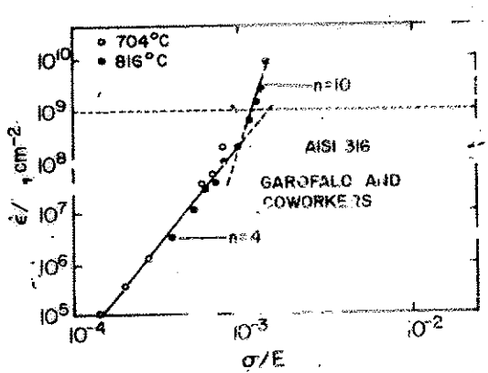

Figure 13.16 Power relationship between $\dot{\varepsilon}$ and σ for AISI 316 stainless steel. (Adapted with permission from S. N. Monteiro and T. L. da Silveira, *Metalurgia-ABM*, 35 (1979) 327)

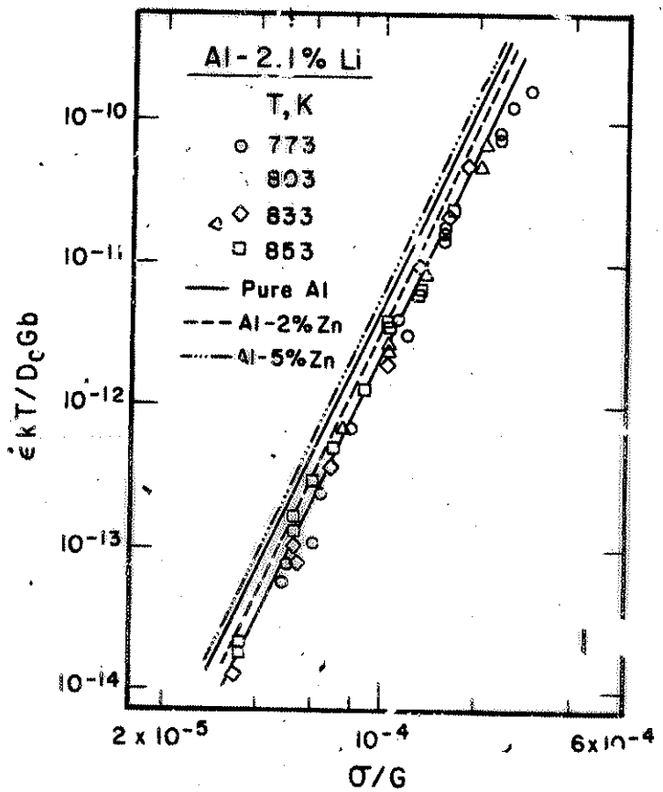

Figure 13.4a Normalized creep rate vs. normalized stress (according to Mukherjee–Bird–Dorn equation) for (a) aluminum, Al–Zn, and Al–Li solid solutions (from K.-T. Park, E. J. Lavernia, and F. A. Mohamed, *Met. Mat.*, 38 (1990) 1837, Figure 11, p. 1844) and (b) various ceramics (from A. H. Chokshi and T. G. Langdon, *Matls. Sci. and Techn.*, 7 (1991) 577, Figure 1, p. 579).

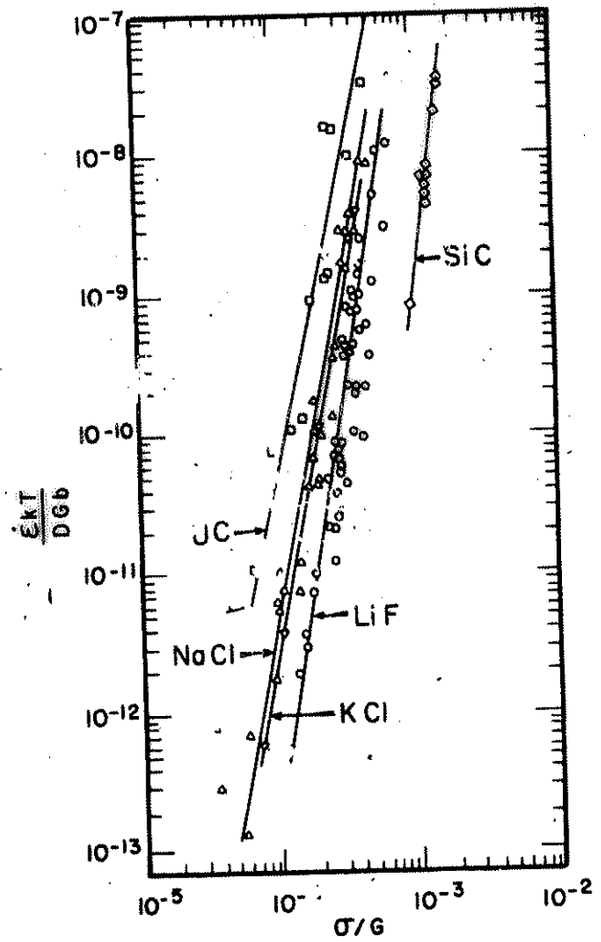

Figure 13.4b

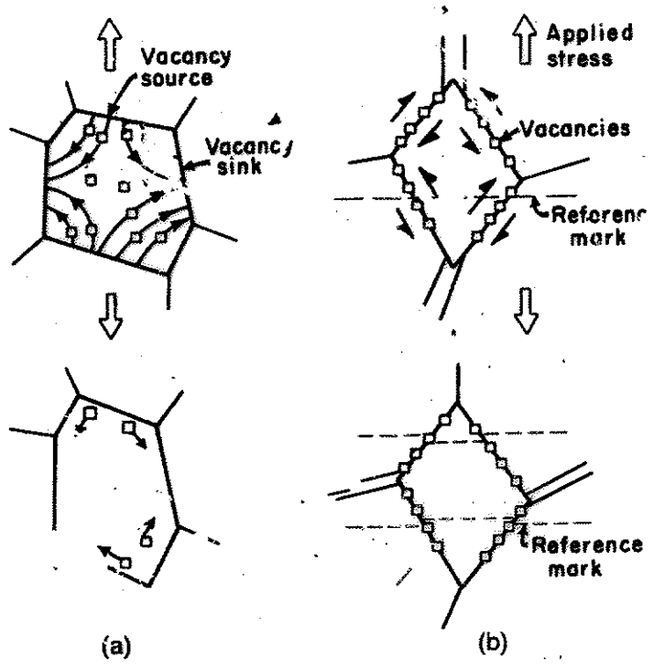

Figure 13.11 Flow of vacancies according to (a) Nabarro–Her ing and (b) Coble mechanisms, resulting in an increase in the length of the specimen.

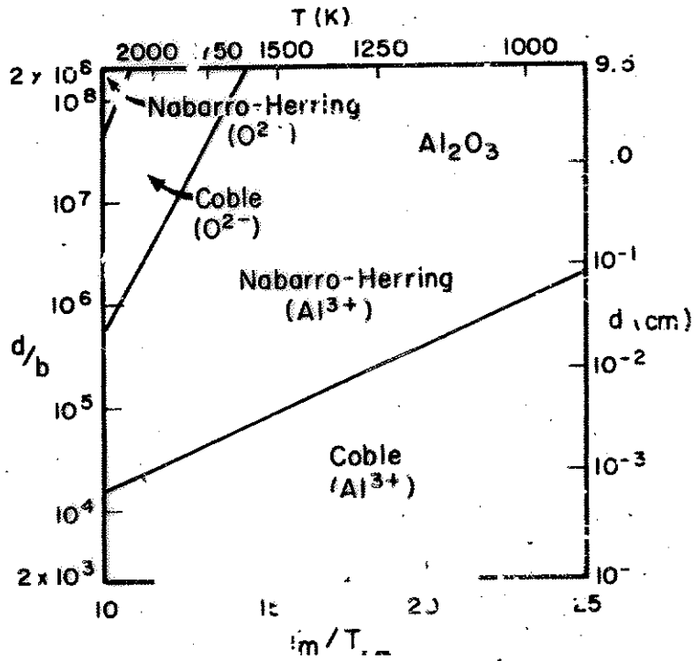

Figure 13.12 Different regimes for diffusion creep in alumina; notice that cations (Al^{3+}) and anions (O^{2-}) have different diffusion coefficients, leading to different regimes of dominance. (From A. H. Chokshi and T. G. Langdon, *Defect and Diffusion Forum*, 66–69 (1989) 1205, Figure 8, p. 1217)

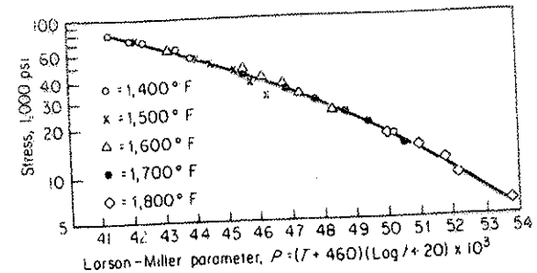

Fig. 13-20 Master curve for Larson-Miller parameter for Astroloy.

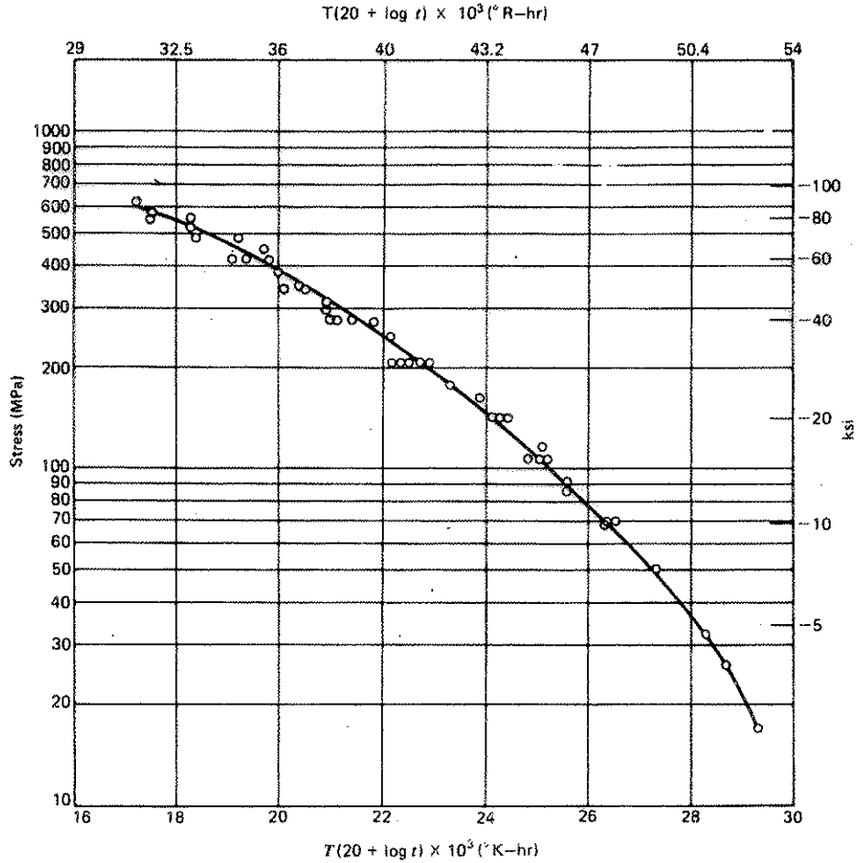

FIGURE 5.25 Larson-Miller plot showing S-590 iron-based alloy data presented in Fig. 5.3.

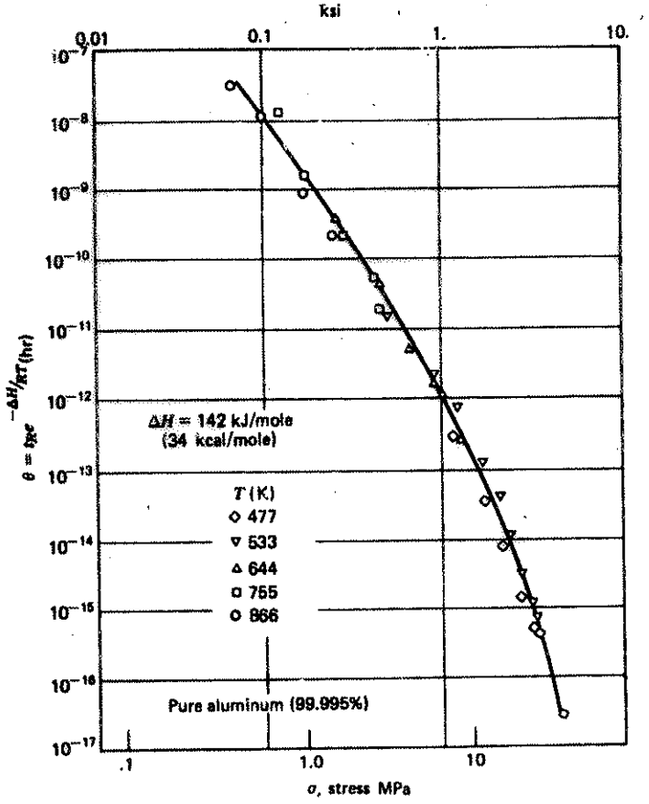

FIGURE 5.28 Correlation of stress rupture data using temperature-compensated time parameter $\theta = t_R e^{-\Delta H/RT}$ for pure aluminum. (From J. E. Dorn,[12] *Creep and Recovery*; reprinted with permission from American Society for Metals, Metals Park, OH, copyright © 1957.)

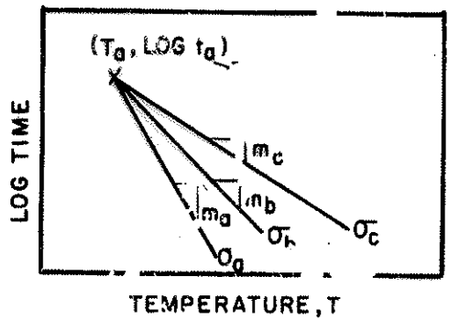

Figure 13.7 Relationship between time rupture and temperature at three levels of stress, σ_a, σ_b, and σ_c, using Manson–Haferd parameter ($\sigma_a > \sigma_b > \sigma_c$).

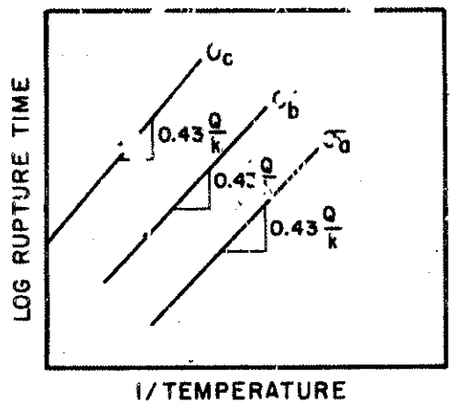

Figure 13.8 Relationship between time to rupture and temperature at three levels of stress, $\sigma_a > \sigma_b > \sigma_c$, using Sherby–Dorn parameter.

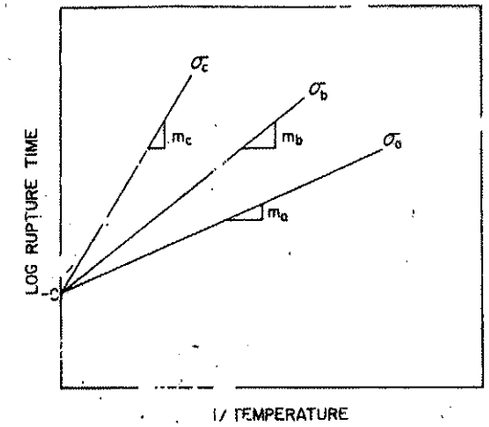

Figure 13.5 Relationship between time to rupture and temperature at three levels of engineering stress, σ_a, σ_b, and σ_c, using Larson–Miller equation ($\sigma_a > \sigma_b > \sigma_c$).

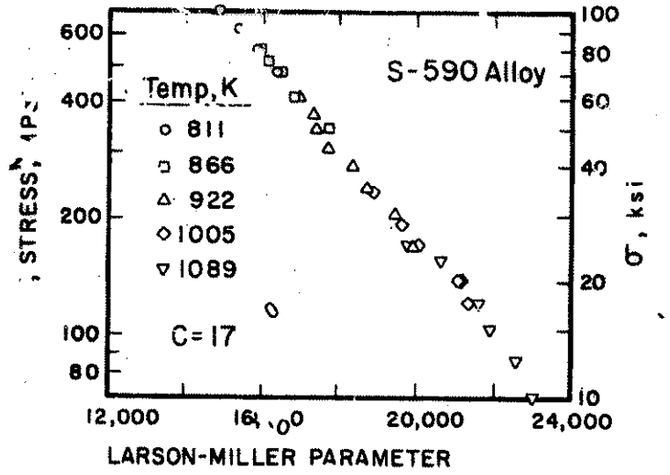

Figure 13.6 Master plot for Larson–Miller parameter for S-590 alloy (an Fe-based alloy) ($C = 17$). (From R. M. Goldhoff, *Materials in Design Eng.*, 49 (1959) 93)

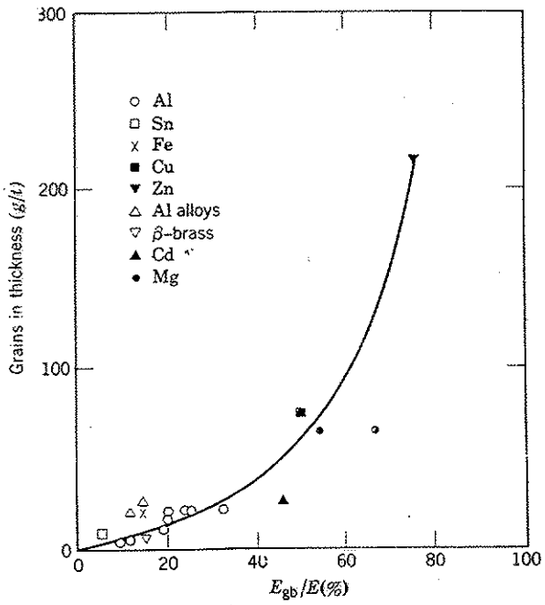

Fig. 6. Dependence of proportion of extension owing to sliding upon number of grains in specimen thickness ($\dot{\varepsilon} \sim 0.1\%/\text{hr}$ and $\tau \sim 0.6$)

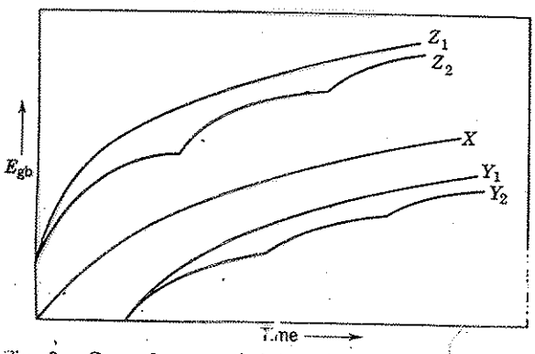

Fig. 3. General types of sliding-time curves found for bicrystals.

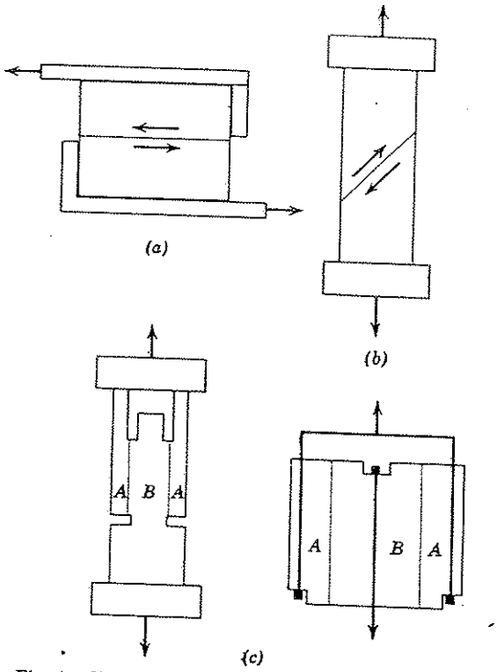

Fig. 1. Types of bicrystal used to study sliding.

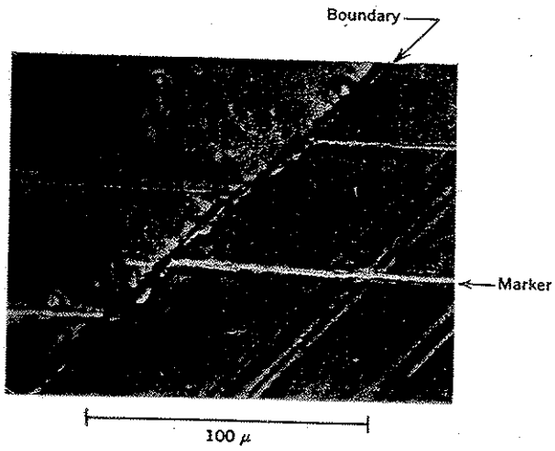

Fig. 2. Sliding at boundary of lead bicrystal. Phase contrast, unetched.

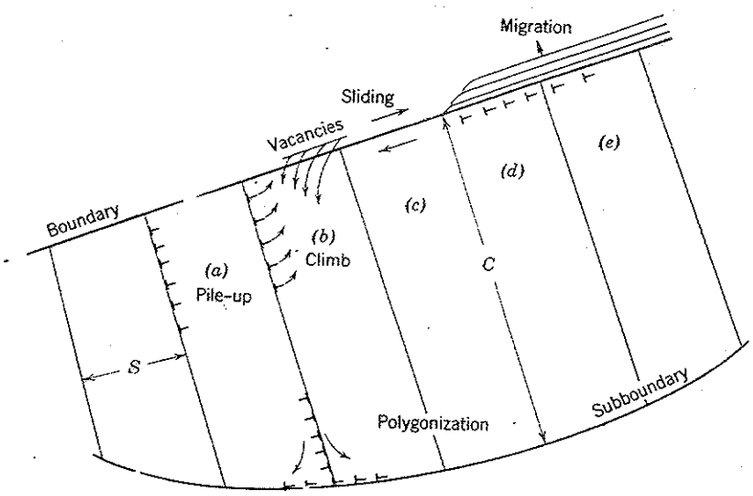

Fig. 8. Sequence of events (a to e) that may lead to boundary sliding and migration. S = slip spacing, C = subgrain diameter.

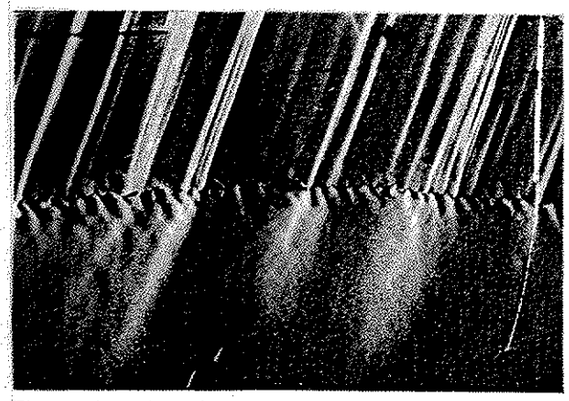

Fig. . Grain-boundary corrugations caused by creep at 400°F and 6800 psi in aluminum-1.9% magnesium alloy. Preliminary creep elongation, 9.4%, followed by repolishing and 10.2% additional elongation. Oblique illumination.

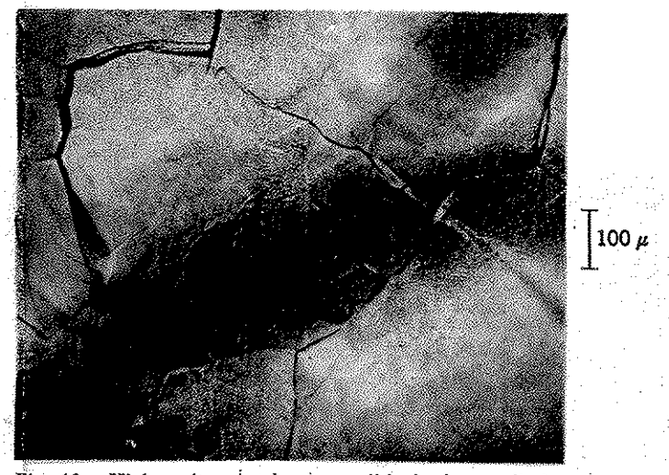

Fig. 10. High-purity aluminum repolished after preliminary creep elongation of 9.8% at 79. °F and 250 psi, then further elongated 1.6% in creep. Oblique illumination.

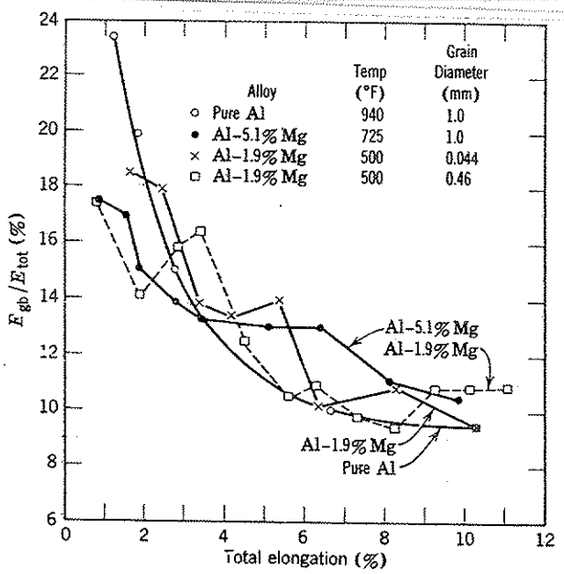

Fig. 4. Variation of ratio of grain-boundary sliding to total elongation as a function of creep strain for aluminum and several solid-solution alloys from 500° to 940°F and for several grain sizes.

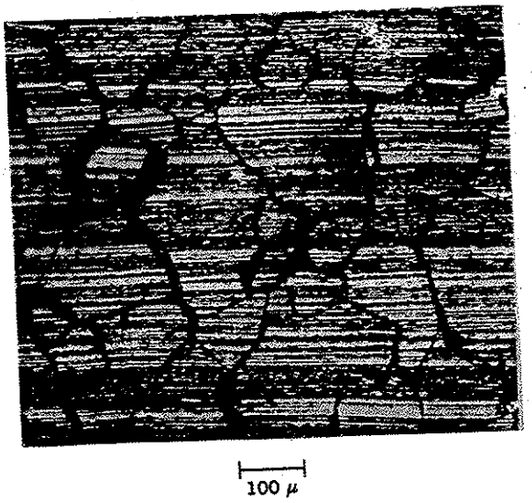

Fig. 5. Rotation and offsets of marker lines on fine-grained lead-tin alloy. 6.3% extension in 190 days.

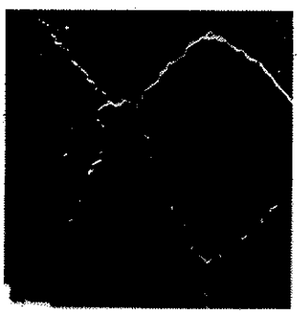

Fig. 7. Corrugated grain boundaries in aluminum-5.1% magnesium alloy after 10.8% elongation at 546°F. Dark-field photomicrograph.

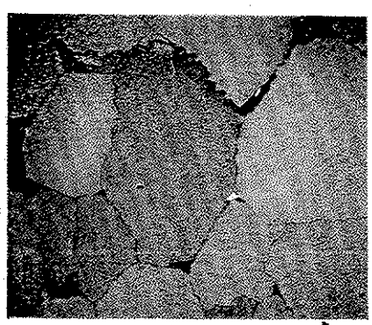

Fig. 8. Aluminum-20% zinc alloy tested in creep rupture at 500°F. Rupture life, 12 hr. Stress direction is vertical.

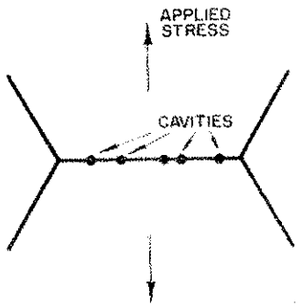

Figure 8.9 *r*-type cavitation at a grain boundary normal to the stress axis.

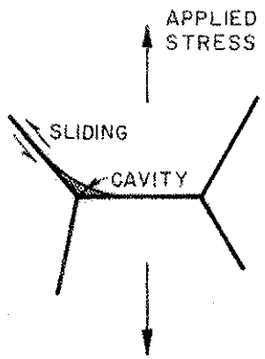

Figure 8.7 w-type cavitation at a grain-boundary triple point.

Figure 8.10 *r*-type cavities nucleated at grain boundaries in copper, seen through an optical microscope.

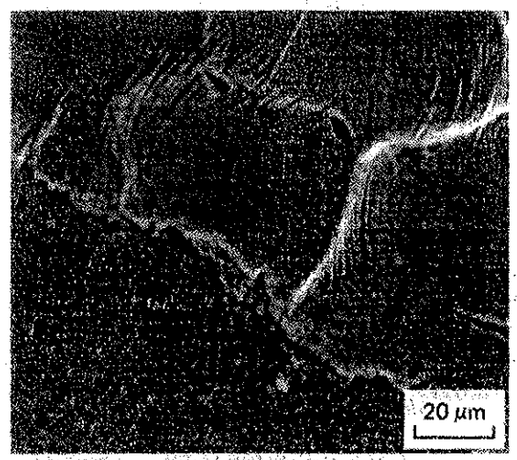

Figure 8.8 w-type cavities nucleated at grain boundaries in copper, seen through a scanning electron microscope.

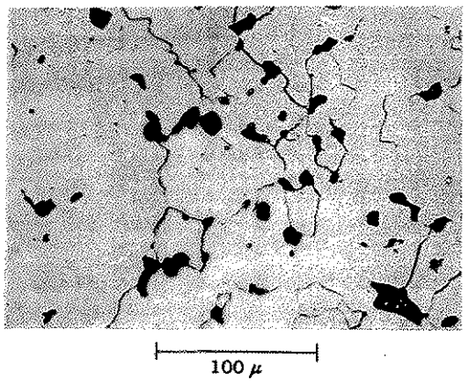

Fig. 12. Cavities in grain boundaries of chromium (27% extension at 3.2×10^{-3}%/hr at 950°C). (After Wilms.[72])

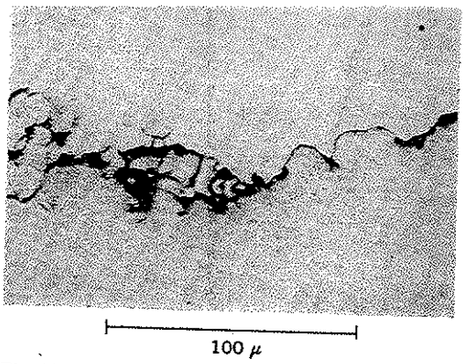

Fig. 11. Cavities in grain boundaries of magnesium (24% extension at 0.2%/hr at 225°C).[63]

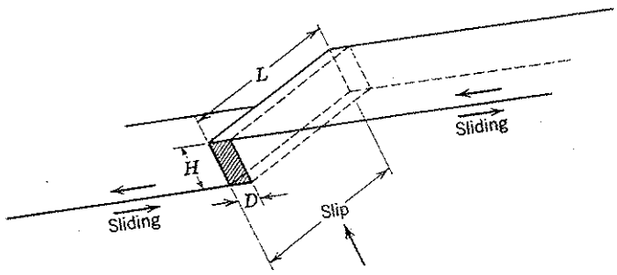

Fig. 17. Formation of an *r*-type cavity by sliding in a grain boundary containing a jog or ledge (here supposed to have been formed by crystal slip).

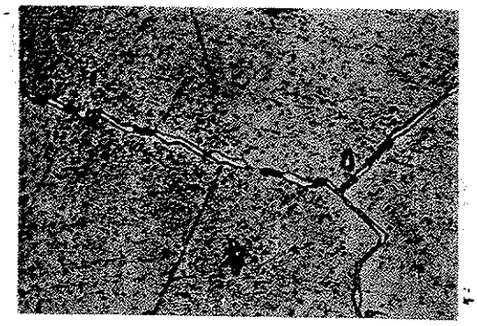

Fig. 14. Cavities and carbide precipitates in a grain boundary of Nimonic 80A-type material (0.5% extension at 5×10^{-3}%/hr at 750°C). (After Weaver, unpublished work.)

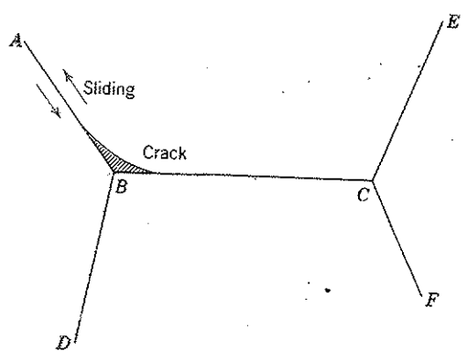

Fig. 16. Zener's mechanism for the formation of a *w*-type cavity at a grain corner.

Fig. 11. Aluminum-2% magnesium alloy tested in creep rupture at 500°F and 4000 psi. Rupture life, 5 hr. Stress direction is vertical.

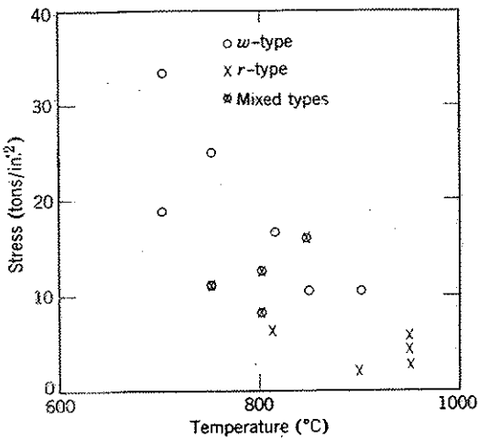

Fig. 13. Dependence of type of cavity upon stress and temperature for Nimonic 90. (After McLean.[74])

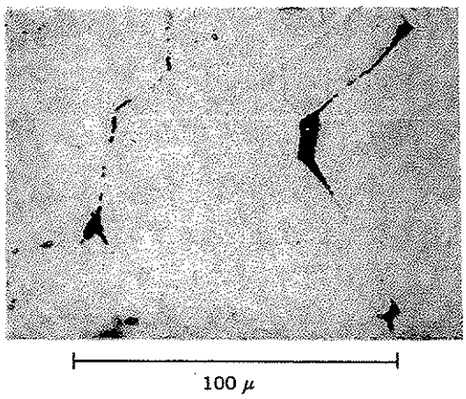

Fig. 10. Cavities in grain boundaries of copper-20% nickel alloy (22% extension at 1.7%/hr at 400°C). (After Reid and Greenwood.[66])

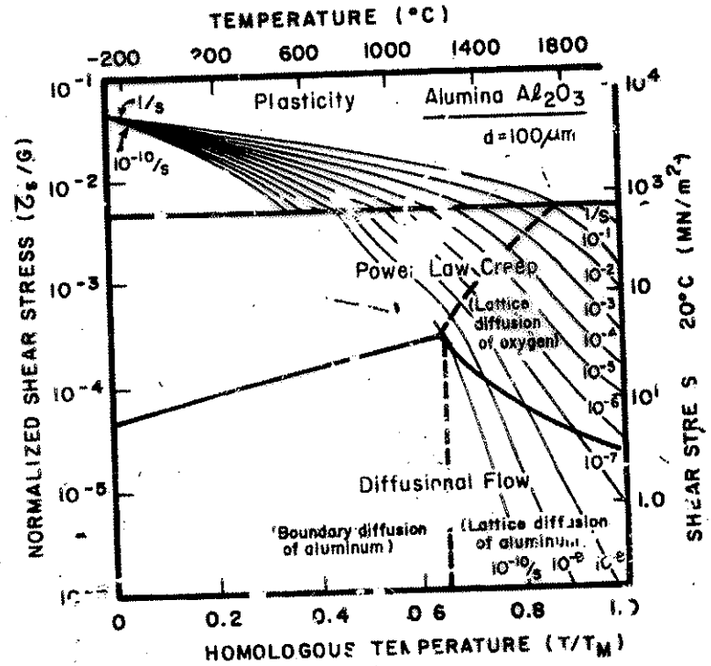

Figure 13.22 Weertman–Ashby map for Al_2O_3 with a grain size of 100 μm. (Adapted from H. J. Frost and M. F. Ashby, *Deformation-Mechanism Maps*, (Tarry Town, NY Pergamon Press, 1982), p. 100, Figure 14.3)

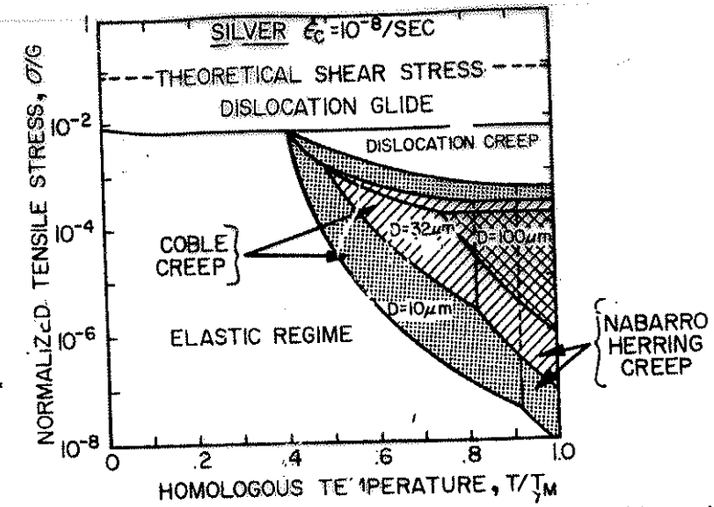

Figure 13.20 Weertman–Ashby map for pure silver, established for a critical strain rate of 10^{-8} s^{-1}; it can be seen how the deformation-mechanism fields are affected by the grain size. (Adapted with permission from M. F. Ashby, *Acta Met.*, 20 (1972) 887)

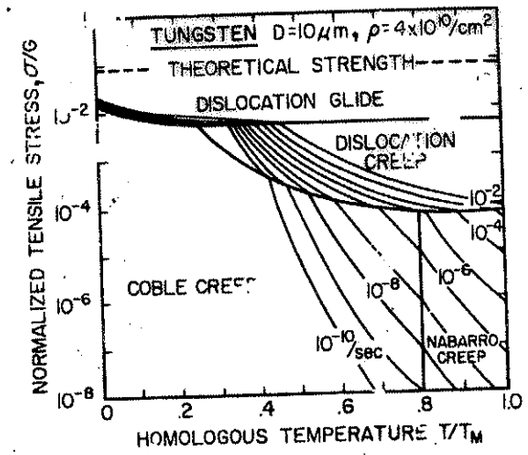

Figure 13.21 Weertman–Ashby map for tungsten, showing constant strain-rate contours. (Reprinted with permission from M. F. Ashby, *Acta Met.*, 20 (1972) 887)

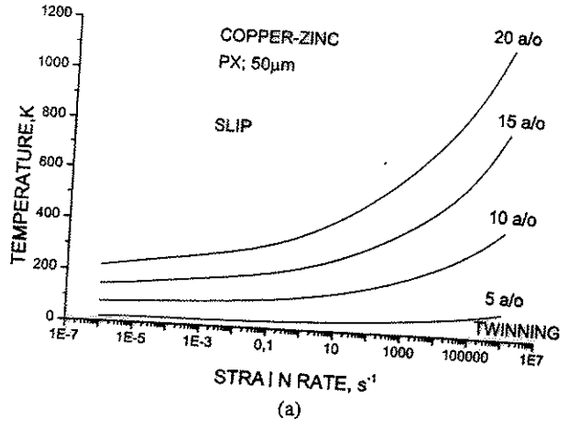

(a)

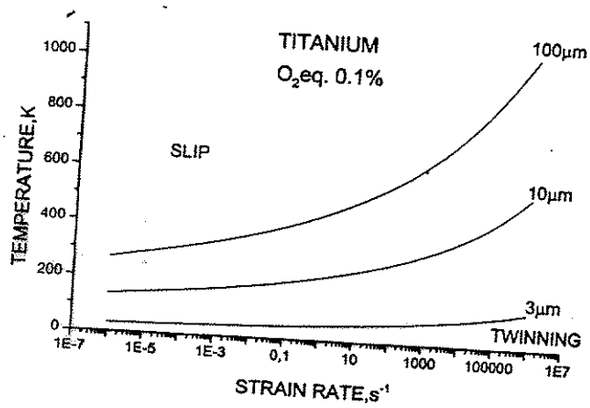

(b)

Fig. 9. (a) Calculated slip–twinning transition for polycrystal Cu–Zn brasses with grain size 50 μm; (b) calculated slip–twinning transition for titanium with different grain sizes

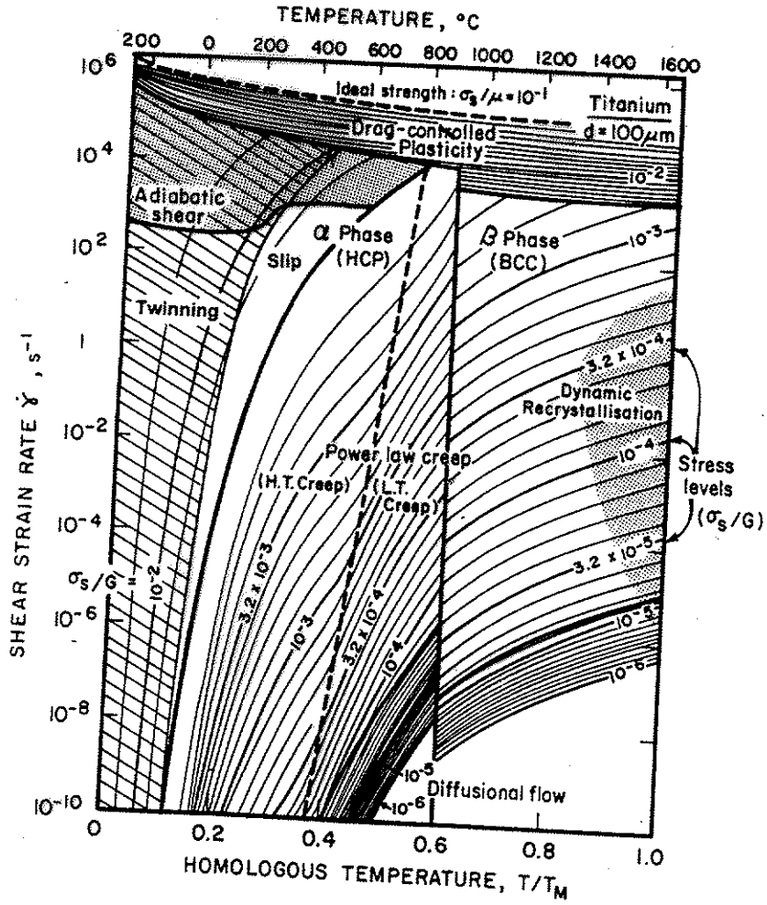

Fig. 10. Weertman–Ashby map for titanium (from Frost and Ashby [57], Fig. 17.4), $d = 100$ μm, in which a twinning domain has been inserted for 0.1% O_2 eq. titanium.

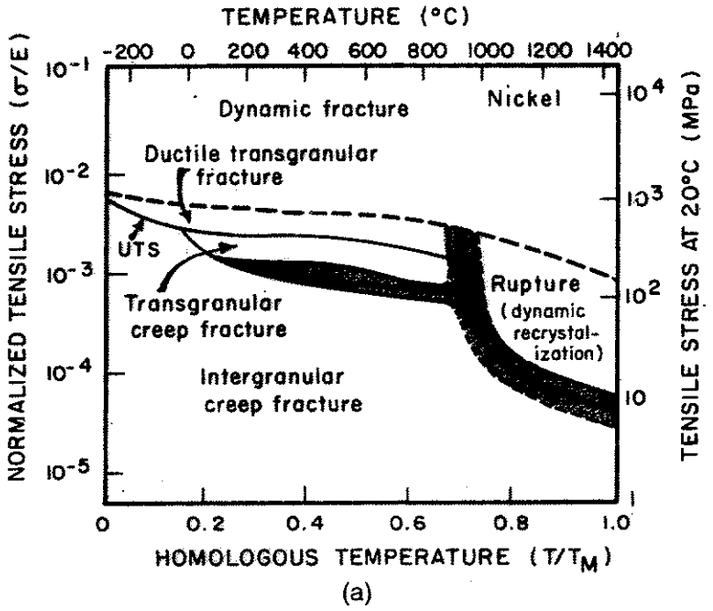

(a)

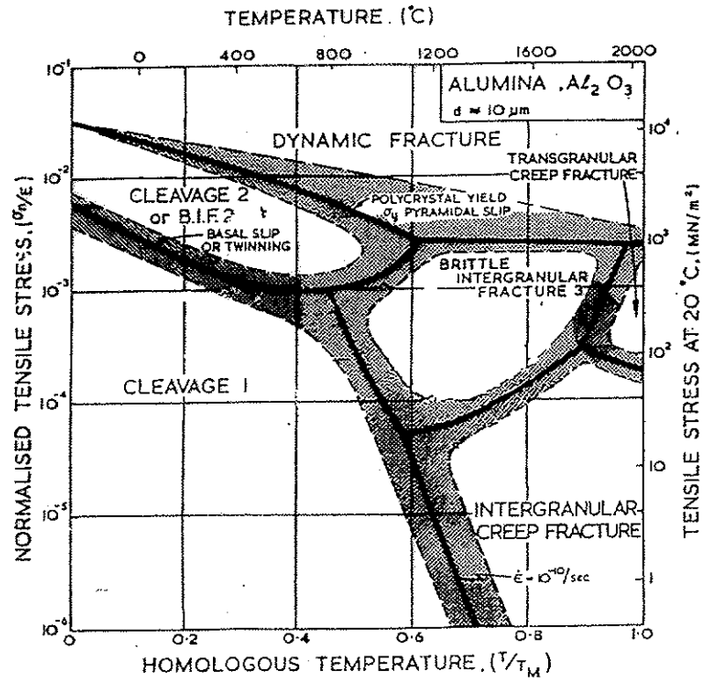

(b)

Figure 8.51 (a) Fracture mechanism map for nickel tested in tension; shading indicates a mixed mode of fracture. (Adapted from M. F. Ashby, G. Gandhi, and D. M. R. Taplin, *Acta Met.*, 27 (1979), 699, Figure 7, p. 707) (b) Fracture mechanism map for alumina with grain size of 10 μm. (Adapted from C. Gandhi and M. F. Ashby, *Acta Met.*, 27 (1979), 1565, Figure 21, p. 1591)

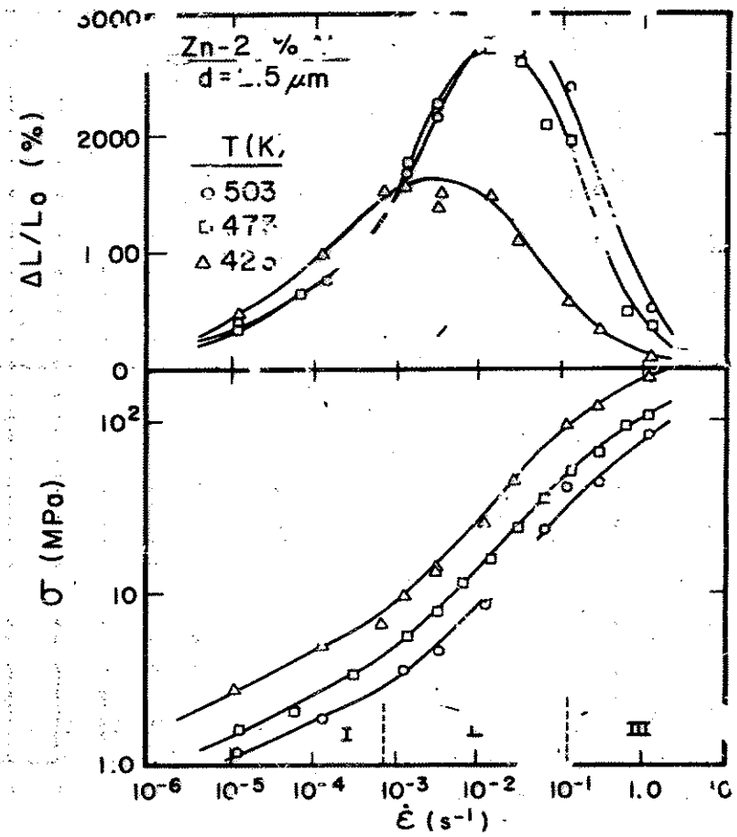

Figure 13.35 Tensile fracture strain and stress as a function of strain rate for Zn–22% Al alloy with 2.5-μm grain size. (After F. A. Mohamed, M. M. I. Ahmed, and T. G. Langdon, *Met. Trans.*, 8 (1977) 9)

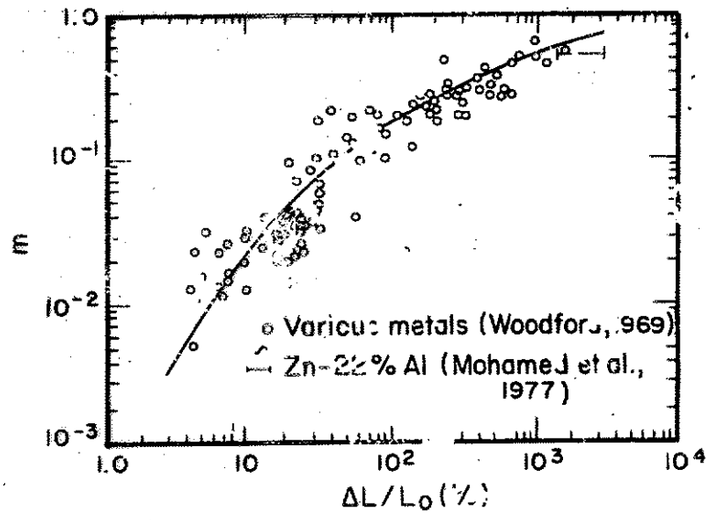

Figure 13.36 Effect of strain-rate sensitivity m on maximum tensile elongation for different alloys (Fe, Mg, Pu, Pb–Sr, Ti, Zn, Zr based). (From D. M. R. Taplin, G. L. Dunlop, and T. G. Langdon, *Ann. Rev. Mater. Sci.*, 9 (1979) 151, 180, Figure 16)

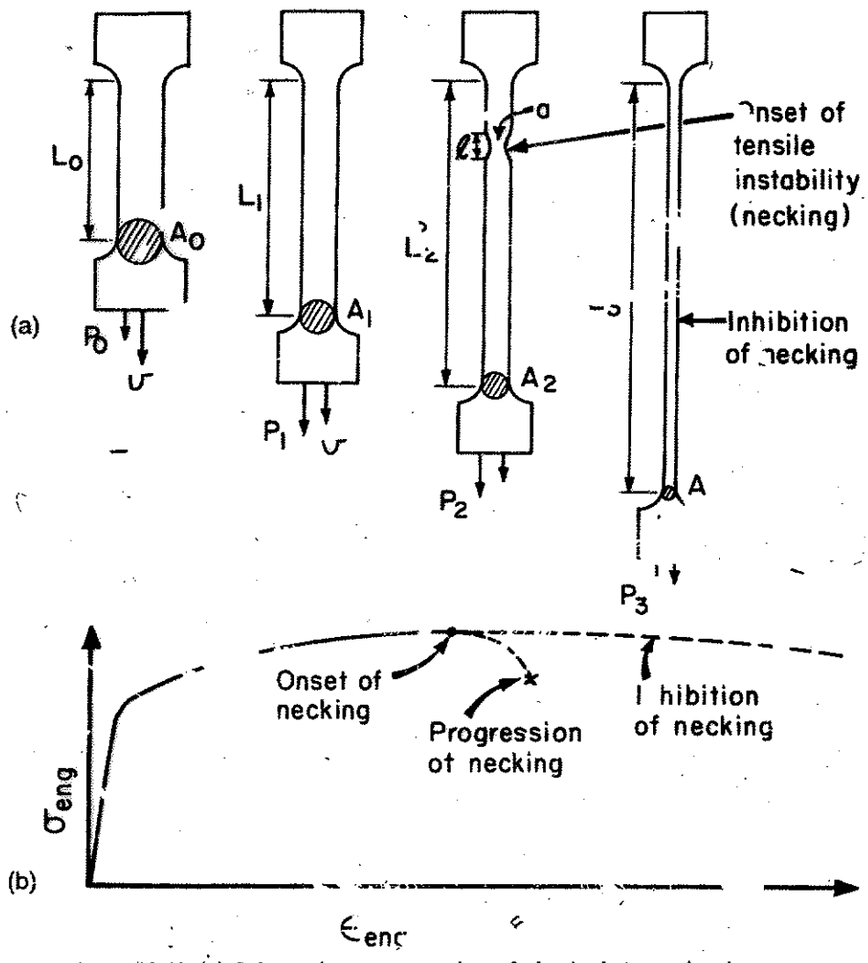

Figure 13.33 (a) Schematic representation of plastic deformation in tension with formation and inhibition of necking. (b) Engineering-stress–engineering-strain curves.

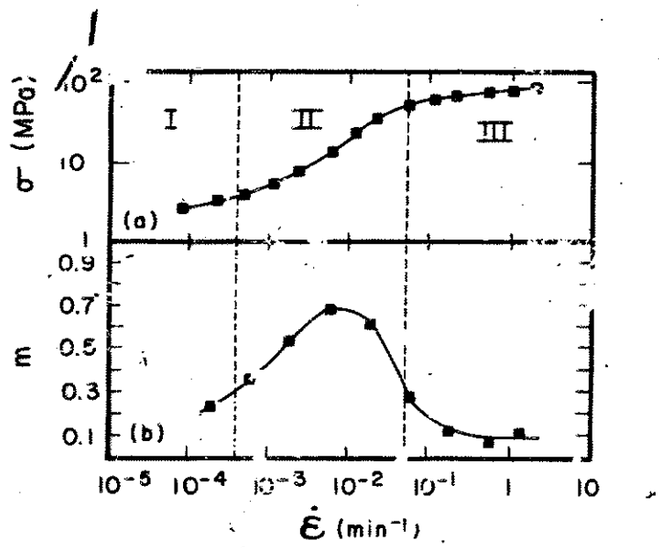

Figure 13.34 Strain-rate dependence of (a) stress and (b) strain-rate sensitivity for Mg–Al eutectic alloy tested at 350°C (grain size 10 μm). (After D. Lee, *Acta. Met.*, 17 (1969) 1057)